Journal of Power Sources 196 (2011) 3592–3603

Contents lists available at ScienceDirect

Journal of Power Sources

journal homepage: www.elsevier.com/locate/jpowsour

Focused ion beam-scanning electron microscopy on solid-oxide fuel-cell electrode: Image analysis and computing effective transport properties

Naga Siva Kumar Gunda [a], Hae-Won Choi [b], Arganthaël Berson [b], Ben Kenney [b,c], Kunal Karan [b,c], Jon G. Pharoah [b,d], Sushanta K. Mitra [a,*]

[a] Micro & Nano-scale Transport Laboratory, Department of Mechanical Engineering, University of Alberta, Edmonton, Canada T6G 2G8
[b] Queen's-RMC Fuel Cell Research Centre, 945 Princess Street, Kingston, Ontario, Canada K7L 5L9
[c] Department of Chemical Engineering, Queen's University, Kingston, Ontario, Canada K7L 3N6
[d] Department of Mechanical and Materials Engineering, Queen's University, Kingston, Ontario, Canada K7L 3N6

ARTICLE INFO

Article history:
Received 29 October 2010
Received in revised form
11 December 2010
Accepted 13 December 2010
Available online 21 December 2010

Keywords:
Solid-oxide fuel-cell (SOFC)
Lanthanum strontium manganite (LSM)
Focused ion beam-scanning electron microscopy (FIB-SEM)
3D reconstruction
Porous medium
Effective transport properties

ABSTRACT

In the present work, microstructural and transport properties of a three-dimensional (3D) microstructure of lanthanum strontium manganite (LSM) are deduced using dual-beam focused ion beam-scanning electron microscopy (FIB-SEM) facility. A series of two-dimensional (2D) cross-sectional images are collected from the LSM sample using FIB-SEM and then reconstructed to 3D structures from the 2D images in a systematic approach. For the first time, the effect of different image processing steps including threshold value, median filter radius, morphological operators, surface triangulation, smoothing filter, etc., on porosity, internal surface area, electronic conductivity and diffusivity are studied. Variation of 33% and 25% on porosity ε and internal surface area S, respectively is observed because of improper selection of threshold value, median filter radius, and morphological operator. The number of triangular surfaces used in 3D reconstructions also varied the porosity ε and internal surface area S by 14.5% and 4.4%, respectively.

Computational domains for calculating effective transport properties are generated using body-fitted cut-cell based finite volume meshes on reconstructed 3D volumes. The normalized effective transport properties are computed on computational domains reconstructed by the FIB-SEM as well as by a numerical model. For the FIB-SEM reconstruction case, the normalized effective properties in z-direction are 25–44% smaller than those properties in x and y directions. This difference is significant and reveals the anisotropy in FIB-SEM reconstructed volume compared to numerically reconstructed volume. The presence of large crater, milling direction and smaller 3D FIB-SEM reconstructed volume could be the main reasons for this local anisotropy.

© 2010 Elsevier B.V. All rights reserved.

1. Introduction

There has been an increasing interest in understanding three-dimensional (3D) microstructures of porous materials such as those used for electrode materials in solid-oxide fuel-cells (SOFC) [1–11] so as to establish structure–property and structure–performance relationships. The accurate determination of effective transport properties such as gas diffusivity, electronic conductivity, and permeability is required for designing highly efficient electrodes for energy conversion devices such as SOFCs [2–5]. Microstructural parameters like fluid–solid interfacial area, particle size distribution, pore size distribution as well as local porosity or material composition are also important in this regard [6–9]. Hence, extracting the desired microstructural information from the porous materials has significant relevance to the fuel cell industry.

Scanning electron microscopy (SEM) is a useful technique for extracting two-dimensional (2D) images of the microstructures but it does not provide the third spatial component (i.e., thickness) of the sample which is important to find interconnected regions and pore volumes, shapes and sizes. Typically, stereological analysis is used to obtain the 3D microstructures and their parameters. In stereological analysis, the feature geometry must be assumed to be that of plates, cylinders, spheres, oblate and prolate spheroids, or other structures according to geometric probability [1]. At the same time, it is difficult to determine these microstructural parameters and measure effective transport properties of a porous electrode material experimentally. Therefore, an alternative approach has been used to construct such structures virtually and to subsequently determine the microstructural and transport properties. Choi et al. [2,12,13], Kenney et al. [3], and Metcalfe et al. [14] numerically constructed the 3D porous electrode structures

* Corresponding author. Tel.: +1 780 492 5017; fax: +1 780 492 2200.
E-mail address: sushanta.mitra@ualberta.ca (S.K. Mitra).

0378-7753/$ – see front matter © 2010 Elsevier B.V. All rights reserved.
doi:10.1016/j.jpowsour.2010.12.042

by using measurable starting parameters such as the particle size distribution. The advantage of such numerical models is that they can quickly generate a desired 3D porous geometry from which important microstructural parameters can be estimated. However, these structures are based on building the electrode geometry using numerical algorithms considering random placement of spheres with some allowance of particle sintering through overlaps. Therefore, these methods are only approximations of the actual physical microstructure of the porous electrodes. Real microstructures need to be produced from the porous materials like SOFC electrodes to compare against the numerical ones and for a better understanding of the microstructural details.

Tomography is one method to generate the realistic 3D images from the 2D sectional images [15]. There has been increasing application of this technique for microstructure characterization of fuel cell electrodes using nano X-ray computed tomography (nano-XCT) [6,16–28] and dual beam focused ion beam-scanning electron microscopy (FIB-SEM) [4,5,8,9,29–34]. Nano-XCT is a non-destructive technique used to characterize the fuel cell electrodes, semiconductors, rock samples, biological samples, etc. [21]. Izzo et al. [17–19,23] used nano-XCT to acquire series of images at spatial resolution of 42.7 nm for 3D reconstruction of SOFC sample with solid YSZ electrolyte and porous nickel–yttria stabilized zirconia (Ni–YSZ) anode layers. In their work, porosity was calculated using voxel count method and tortuosity was evaluated by solving Laplace equation. They validated volume fraction calculations with mercury intrusion porosimetry. Lattice Boltzmann Method (LBM) was also used to estimate the depletion of fuel gas in the fuel cell electrode. Grew et al. [24] have also investigated the structure of Ni–YSZ anode using nano-XCT with a spatial resolution of 38.5 nm. They extracted tortuosity, contiguity and pore sizes and then compared their results with LBM of Izzo et al. [18]. Shearing et al. [6] have also reported the nano-XCT study to understand the structure of the Ni–YSZ electrode material. They performed nano-XCT at varying length scales of Ni–YSZ sample and compared their structural details with FIB tomography. Gaun et al. [27,28] studied the structure of LSM–YSZ and Ni–YSZ SOFC composite electrodes using nano-XCT. The results obtained in their work were used to quantify structural parameters like volume ratio of three phases, connected porosity, surface area of each phase, etc. However, this nano-XCT technique has a significant short-coming in that a very small sample is required to obtain high resolution images, which is often in the order of millimetre dimensions or even smaller. Such limitations in sample size can be overcome by using a FIB for the sample preparation [6]. Ostadi et al. [10] studied the 3D reconstructed images for gas diffusion layer (GDL) and a microporous layer (MPL), relevant to Proton Exchange Membrane (PEM) fuel cells. They created a 3D image of the GDL–MPL assembly through nano-XCT with a 680 nm pixel resolution for the GDL and FIB-SEM with 14 nm pixel resolution for the MPL. They determined the critical nano-structural features like porosity, characteristic lengths and 3D pore size distribution directly from 3D images. They also computed the tortuosity and permeability of the MPL using LBM.

FIB, a destructive imaging technique, first came into existence two decades ago for nano-machining, depositing and imaging semiconductor materials. It is a well-established technique to generate 3D microstructures of porous material with resolutions of nanometres and without any dependence on sample size [8,9,35]. FIB tomography is very useful for studying SOFC microstructures, since most SOFC electrodes have nano-scale pores. Wilson et al. [4,5,8,9] have demonstrated FIB-SEM by studying the microstructure of composite electrodes such as Ni–YSZ cermet anodes, LSM–YSZ cathodes, and $(La,Sr)CoO_3$ cathodes using dual-beam FIB-SEM facility. To aid in the analysis of composite electrodes, Wilson et al. [4,5] used an impregnated sample with an epoxy to discriminate different phases in the images and used inlens detectors for capturing back-scattered electrons in the images. Wilson et al. [8] extracted the macroscopic electrode parameters such as interface areas and triple-phase boundaries (TPB) from the 3D microstructural data. They also discussed the calculation of critical microstructural features such as volume fractions and surface areas of specific phases, TPB, and the connectivity and tortuosity of specific subphases within SOFC anode (Ni–YSZ) [9]. In a similar study, Wilson et al. [5] reported the 3D characterization and quantification of important structural parameters from LSM–YSZ cathode and identification of LSM–YSZ–pore three-phase boundaries. They also studied the effect of composition of cathodes on performance of SOFC by correlating the 3D microstructure and polarization resistance [4]. In the present study, similar to Wilson's set-up, the FIB-SEM is used to record the 2D sectional images of lanthanum strontium manganite (LSM), a typical cathode material of SOFC.

Following the FIB-SEM work reported by Wilson et al., there has been a growing interest on characterization of the microstructure of electrode materials by various techniques and subsequent extraction of micro-structural property information. Kenney et al. [3] computed the TPB length, surface area and pore size from numerical reconstruction of composite SOFC electrodes. They found that the TPB length evaluated for mono-sized particles with same mean particle sizes was as much as 40% higher compared to real particle size distributions. Iwai et al. [11] also evaluated the TPB length density and tortuosity factors from SOFC anode (Ni–YSZ) using the dual-beam FIB-SEM equipped with an energy dispersive X-ray spectroscopy (EDX) unit. They estimated the TPB density using the centroid and volume expansion methods and tortuosity factors with lattice Boltzmann and random walk methods. They observed the excellent agreement between the two methods used for calculating each parameter.

As elucidated in this previous paragraph, there is a significant interest by different research groups to compute micro-structural properties from the images derived from FIB-SEM studies. Notwithstanding the challenges in fine-tuning of the experimental parameters to generate high quality 2D data, the procedure for the post-processing of images to generate representative 3D structure and the methodology for subsequent generation of a mesh for the computation of transport properties affect the final outcome. Processing of images is required before stacking the 2D images to obtain a 3D reconstructed image and obtaining the microstructural parameters like porosity, composition, feature size, shape and connectivity. The processing steps like image registration, algebraic operations, morphological operations, filtering and segmentation, etc., are required prior to 3D reconstruction to align the images; to remove any noise and to label the different phases. Recently, Joos et al. [34] described the effect of image processing steps on the calculation of surface area, volume/porosity fraction and tortuosity. Their work is mainly focused on the selection of proper threshold value to differentiate the pore space and solid matrix. In the present work, we examine the effect of different image processing steps in calculating porosity, internal surface area, diffusivity, etc. A number of statistical [36–40] and process-based [38,41] models are developed for reconstructing 3D images from 2D thin section images. In the present study, a modified and improved marching cubes algorithm [42–46] is used for generating 3D reconstructed images. However for calculating effective transport properties, we converted 3D reconstructed microstructures into body-fitted cut-cell based finite-volume meshes using MicroFOAM [12], which is a suitably modified version of the open-source CFD code OpenFOAM® [47].

The existing body of literature on extraction of microstructure of porous material, like LSM, using FIB-SEM seldom describes the impact of various image processing steps and algorithm on the phase differentiation, in particular the porosity and internal surface areas. The main focus of this paper is to describe a system-

atic approach in quantifying the processed images from FIB-SEM and subsequently computing the transport properties of porous electrode, like electronic conductivity and diffusivity. Further, a systematic analysis is reported for the first time in this work, where the effects of various image processing steps including threshold value, median filter radius, morphological operators, surface triangulation, smoothing filter, etc., are demonstrated on the computed porosity, internal surface area, electronic conductivity and diffusivity. A sensitivity study is also performed where the computed transport properties are compared between those obtained from reconstructed FIB-SEM images and the numerical reconstructed images assuming random structures.

2. Materials and methods

2.1. Sample preparation

The porous cathode was deposited using $(La_{0.8}Sr_{0.2})_{0.95}MnO_{3\pm\delta}$ powder (LSM, Praxair) onto a thick $(Y_2O_3)_{0.08}(ZrO_2)_{0.92}$ (YSZ, Tosoh) electrolyte disk. The LSM powder particle size was determined from a light scattering technique to have a mean diameter of 0.73 μm with a standard deviation of 0.3 μm. First, the YSZ powder was pressed in a steel die set using a Carver 10 ton press at a pressure of 15,000 psi. The electrolyte disk was then sintered to 1400 °C for 5 h. Once cooled, the electrolyte surface was polished with 240, 400 and 600 grit silicon carbide paper and re-fired to 1400 °C. After the sintering processes, the dimensions of the electrolyte were found to be approximately 12.9 mm in diameter and 0.7 mm thick. Next, LSM powder was mixed with ethanol, poly(vinylpyrrolidone) and 5 mm diameter YSZ milling media and the mixture was ball milled for 20 h. The resulting LSM ink was then pulse sprayed using an automated air-brush onto the YSZ disk. The combined electrode/electrolyte was then sintered to 1150 °C for 2 h.

The porosity of electrodes fabricated using this method was estimated from:

$$\varepsilon = 1 - \frac{\rho^{\text{eff}}}{\rho^{\text{bulk}}}, \quad (1)$$

where ρ^{eff} is the effective density of the electrode, estimated based on the volume of the electrode and the deposit weight, and ρ^{bulk} is the bulk density of an LSM particle, equivalent to the electrode density for an electrode with zero porosity. The thickness of the sintered electrode was 16 μm, measured from an SEM cross-section image, the deposit weight of the electrode was 7.1 mg and the bulk density was 6.39 g cm^{-3}. With these properties, the average porosity of the electrode was estimated to be 42.5%.

2.2. Acquisition of 2D images from FIB-SEM

Here we describe the steps followed to obtain FIB-SEM images. First, a layer of 10 nm chromium and 40 nm gold was sequentially deposited onto the LSM electrode sample using a planar magnetron sputtering system. Then, the top surface of the sample was inspected using a Zeiss N-Vision 40 crossbeam workstation. The N-Vision 40 has the capability of doing both FIB milling and SEM imaging, and is therefore known as a dual-beam FIB-SEM facility. Next, a trapezoidal trench of width 19.97 μm, height 34.09 μm, depth 25 μm and base angle 30° was milled into the LSM sample under an accelerated voltage of 30 kV and a milling current of 27 nA. This trench helps in better exposure of the section of interest and contrast adjustment purpose at the time of taking series of cross-sectional SEM images. Fig. 1(a) shows the location of the section considered on the LSM sample and Fig. 1(b) shows low-magnification image of LSM sample with a trench. Thereafter, a layer of 1 μm platinum was deposited on the LSM sample surface for a rectangular area of 11.94 μm width and 12 μm height as shown in Fig. 1(b) under an accelerated voltage of 30 kV and a milling current of 300 pA using deposition mode of the N-Vision 40 system. The purpose of this platinum layer was to correct the tilt and alignment while taking the serial sectioning images into consideration. Next, the electron beam was used to image the side wall of the trench (platinum coated side) at an angle of 54° from the parallel to the side wall. A trapezoidal area of width 8.99 μm, height 8.99 μm and base angle 20° was selected on the platinum coated surface for milling the surface for taking the serial sectioning images. Then a 40 nm thick layer was milled in the selected area under an accelerated voltage of 30 kV and a milling current of 700 pA. A series of 2D images of 10.94 nm resolution were collected from the LSM sample by milling the sample layer by layer. A set of 157 images were collected. Fig. 1(c) shows the top view of the trench and milled volume from low resolution to high resolution. The bottom surface of the milled volume was found to be not perfectly smooth, as observed from the enlarged view in Fig. 1(c). Fig. 1(d) depicts the trench and milled volume at an angle of 55° from the sample table to FIB milling direction. The serial section of slice number 151 is shown in the enlarged figure, in which grey colour indicates the LSM solid matrix and black colour indicates the pore space. The images shown in Fig. 1 were obtained using the secondary electron signal detector. Imaging with the electron beam was done at voltages around 2–5 kV whereas milling of trenches was performed with Ga ion beam operating up to 30 kV and a beam current of 27 nA. These beam currents and voltages are optimized for LSM sample for minimizing the charging effect and electron/ion beam damage to surface. The penetration of Ga ions can be checked using open source software: SRIM (The Stopping and Range of Ions in Matter). If the ion beam operates at voltage and current greater than 30 kV and 27 nA, the sample becomes amorphous due to the penetration of Ga ions. Ga ions may penetrate up to 20–40 nm within the substrate. This is more of a concern for really thin samples (TEM work) [1].

2.3. 3D stacking or reconstruction

A 3D reconstruction of the porous LSM structure was obtained by stacking the 2D cross sectional SEM images in 3D space. In this work, most of the image processing and 3D reconstruction was carried out using the Avizo Fire edition version 6.2 and XSkeleton extensions (VSG, Visualization Sciences Group, Inc., Burlington, MA). Pre-processing of images was required to get a good quality 3D reconstruction. The first step in creating 3D microstructure involves alignment of collected serial sectioned 2D images using some fiduciary markers as objects of reference. Fiduciary marking (reference points) used for alignment of images is shown in Fig. 1(e). Four points were located outside the milled volume on the images as fiduciary markers and these points were then adjusted to place all images at the common point of observation. After executing this fiduciary marking alignment, least-square algorithm is used once again for alignment to remove any errors in the alignment based on grey values. Proper alignment of images without down sampling was required while stacking the images to get accurate 3D reconstruction. A volume of 9.12 μm × 4.75 μm × 4.08 μm was selected from the 3D data. The selected volume should be available in every aligned images starting from the first image to last sectioned image. Since the resolution and contrast in the sectioned images were reduced progressively from the first to the last section, a process for changing the range of pixel intensity values, i.e., normalization process was carried out. The normalized image of slice 51 is shown in Fig. 2(a). Then, the normalized image was processed to find different phases of the sample by segmentation process. The segmentation process consists of separating and identifying the different segments of a digital image based on the intensity of its pixels. This step is carried out by adjusting the threshold of the

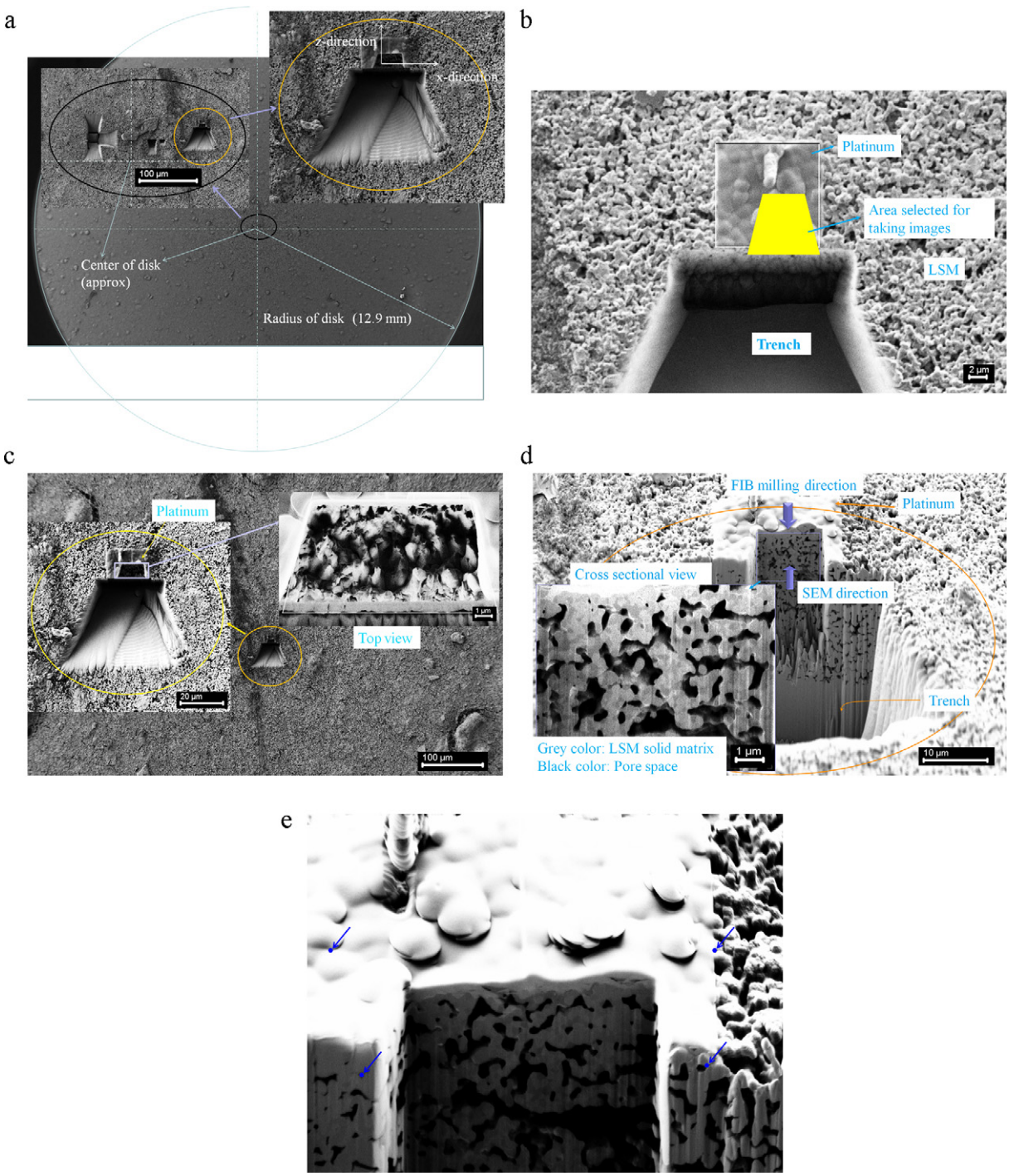

Fig. 1. Low-magnification image of LSM sample: (a) location of section considered in the LSM sample; (b) trench in the sample is shown at stage angle of 54° along with the region showing the platinum coated surface, this portion of this coated surface is taken for milling the material for 3D reconstruction; (c) the top view of the trench along with the volume taken for 3D reconstruction; enlarged view in the left shows the high resolution image of the same area and the enlarged view in right shows the bottom surface of region taken for reconstruction after milling; (d) the cross-sectional view of the milled surface taken for reconstruction; and (e) the fiduciary marks used for alignment of series of images.

pixel intensity values. In this set of images, the threshold value was kept as 60, i.e., pixel intensity value. The pixels that are below 60 in the image were kept as black and the pixels which are in the range of 60–255 were kept as white. The black colour in the segmented image as shown in Fig. 2(b) indicates the pore and the white colour indicates the solid matrix (grain), that means two phases in the images were labeled as pore (void) space and solid matrix, respectively. Nonlinear digital filtering methods such as 3D median filter was then used to reduce the noise in images. This process improved the edge detection on all images which is helpful for the subsequent processing stages. Further, the smoothing of images was carried out to reduce the noise within an image and thus produce a less pixelated image. Fig. 2 shows the change in the image of slice number 51 after processing, as described here. Comparing the bottom left corner of normalized image (Fig. 2(a)) and the image resulting after smoothening steps described here (Fig. 2(e)), it appears that certain portion of the solid matrix is incorrectly assigned as a pore space. Due to presence of dual beam imaging artifacts, such as

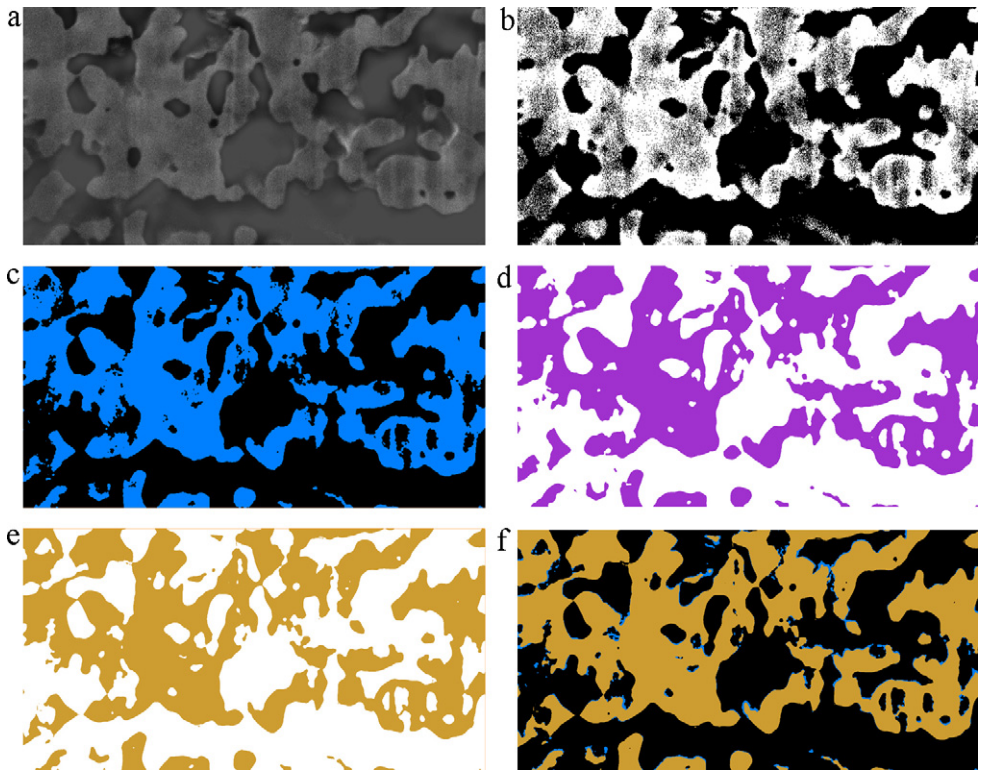

Fig. 2. Steps used in preprocessing the images before reconstruction is shown on cross sectional image of slice number 51: (a) grey scale image after normalization process which has been corrected for shadowing, where pore space is dark and matrix is bright; (b) binary image computed by thresholding the image in A, where pore space is black and matrix is white; (c) binary image computed by applying median filter to image in B, where pore space is white and matrix is blue; (d) surface cut of 3D reconstructed image after stacking using marching cubes algorithm, the blue colour indicates the solid matrix and transparent colour indicates the pore or void space; (e) surface cut of 3D reconstructed image after applying smoothing filter to remove the noise in the image and edges; and (f) the difference in the pore and solid matrix phases before applying smoothing filter and after smoothing filter on 3D reconstructed image. (For interpretation of the references to colour in this figure legend, the reader is referred to the web version of the article.)

curtaining, detector noise, the normalized image does not clearly represent the actual surface morphology of the slice. It is to be noted that in the present study, the sample was not infiltrated by epoxy. In some cases, infiltration is a better option because it can give better contrast and prevents the solid phase, which may be out of the measurement plane, to appear in the images. Infiltration does not change the segmentation needs, it merely brings in more "greylevel resolution" between pore and solid (electrode) phase. The method of visual inspection used in our study yields a satisfactory segmentation so that infiltration was not necessary in our case. Segmentation methods such as level set method [48] might provide more accurate segmentation but at the expense of a considerable increase in computational requirements. Avizo also provides such method with watershed segmentation (which is usually applied to the image gradient) as a robust and community-accepted alternative. Since the sample has only two phases, segmentation based on threshold value is more appropriate and easy method to apply. In addition, we applied median filter and smoothing filter for satisfactory segmentation to remove segmentation errors.

Stacking of the processed images can give the 3D reconstructed image of LSM sample. An improved marching cubes algorithm was used for extracting a polygonal mesh of an isosurface from a 3D voxels data [42–46]. This was an inbuilt algorithm available in the Avizo Fire edition, in which the 3D data was processed in scan-line order and calculated triangle vertices using linear interpolation to create triangle models of constant density surfaces, i.e., polygonal isosurfaces [42]. Fig. 3 represents the cross sectional view of 3D reconstructed sample in three directions. The coloured part shows the LSM solid matrix and transparent part represents the pore space.

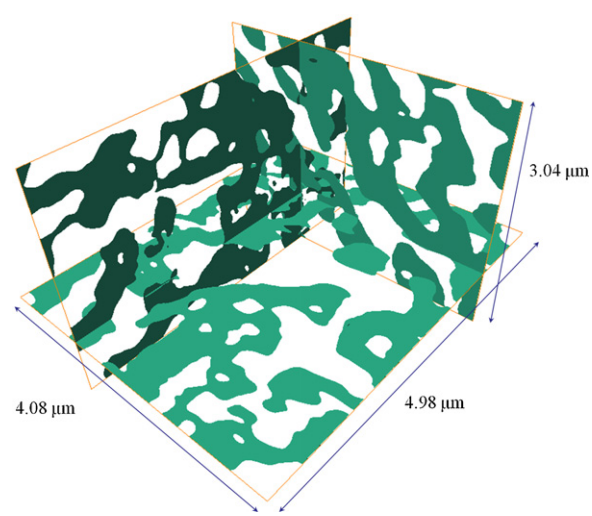

Fig. 3. Three different cross sectional views of the 3D reconstructed sample.

2.4. Calculation of effective transport properties

The net transport of a species within a composite structure, although governed by the intrinsic transport coefficient, is modified due to the tortuous pathways and the presence of blocking phases within a porous volume. Thus, the effective transport coefficient (α^{eff}) for a composite material can be related to the intrinsic transport coefficient via some function of the volume fraction of the pertinent phase responsible for the transport. The functionality

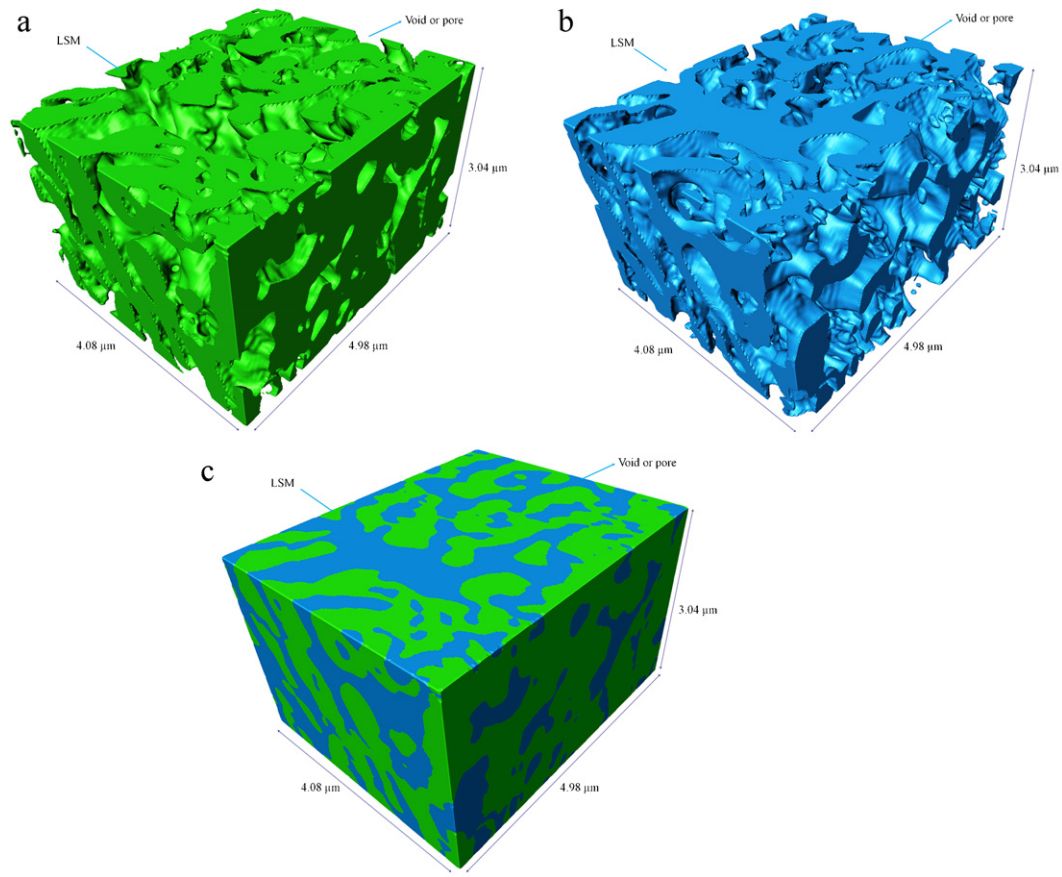

Fig. 4. Reconstructed 3D microstructure of LSM sample: (a) 3D reconstruction showing the solid matrix of LSM sample in coloured part and other pore space in transparent; (b) 3D reconstruction of pore-network structure showing the solid matrix of LSM sample in transparent and other pore space with colour; and (c) 3D reconstruction showing the solid matrix of LSM sample in green colour and pore space in blue colour. (For interpretation of the references to colour in this figure legend, the reader is referred to the web version of the article.)

depends on the microstructure. To accurately compute the effective transport properties for our sample, the 3D reconstructed volumes of the solid LSM phase and pore spaces were converted into body-fitted cut-cell based finite-volume meshes using MicroFOAM [12], which is a suitably modified version of the open-source CFD code OpenFOAM® [47].

Transport of the electrons and gas species within the phase domains of the electrode sample is assumed to be dominated by diffusion process. For each phase, the relevant potential field ϕ is governed by the diffusive processes as follows:

$$\nabla \cdot (\alpha \nabla \phi) = 0, \quad \phi \in \Omega_{\text{phase}}, \tag{2}$$

where α denotes the bulk diffusion coefficient and Ω_{phase} is the computational volume for each phase. Note that each phase volume (Ω_{phase}) is embedded in the electrode sample volume (Ω) so that $\Omega = \Omega_{\text{LSM}} \bigcup \Omega_{\text{pore}}$. Dirichlet (fixed value) boundary conditions are imposed on the top and bottom boundaries of each phase, i.e., $\phi_{\text{top}} = 1$ and $\phi_{\text{bot}} = 0$. Symmetry (zero gradient) boundary conditions, i.e., $(\partial \phi / \partial n) = 0$, are presumed on the sides of each phase boundaries as well as solid and pore phase interfaces. To solve the diffusion equation (i.e., Laplace equation) of the applied potential field (ϕ) for each phase domain Ω_{phase}, the finite volume method (FVM) was used. From the solution of the diffusion equation in Eq. (2), the effective transport coefficient for gas diffusion (D^{eff}) and the effective electronic conductivity (κ^{eff}) can be obtained.

The local transport flux q for each phase can be related to the generalized local concentration gradient such that

$$q = \alpha \nabla \phi, \tag{3}$$

where the potential field ϕ is calculated from Eq. (2). The average (surface integrated) local flux across the surface boundary of each phase should be satisfied such that

$$\int_{\partial\Omega} \alpha^{\text{eff}} \frac{\partial \phi}{\partial n} dS = \int_{\partial\Omega_{\text{phase}}} \alpha \frac{\partial \phi}{\partial n} dS. \tag{4}$$

Hence the normalized effective transport coefficient can be evaluated by

$$\frac{\alpha^{\text{eff}}}{\alpha} = \frac{\int_{\partial\Omega_{\text{phase}}} (\partial \phi / \partial n)\, dS}{(\Delta \phi / L) S}, \tag{5}$$

where $\Delta\phi$ represents the potential difference, L is the selected height of the computational domain and S denotes the selected boundary surface area of each phase. Note that $(\alpha^{\text{eff}}/\alpha) = (D^{\text{eff}}/D)$ represents molecular diffusion ratio for the pore phase and $(\alpha^{\text{eff}}/\alpha) = (k^{\text{eff}}/k)$ represents electrical conductivity ratio for the LSM phase.

3. Results and discussions

Fig. 4 shows the resulting 3D reconstructed image produced after stacking the 2D images taken from dual-beam FIB-SEM system. Only a reduced box shape domain of 4.98 μm × 3.04 μm × 4.08 μm is displayed for illustration. The coloured part in Fig. 4(a) is the LSM solid matrix and the transparent part is pore space. The image illustrates the 3D microstructure of LSM and pore spaces, and their local surface curvatures. A better representation of the pore space is shown in Fig. 4(b) where the

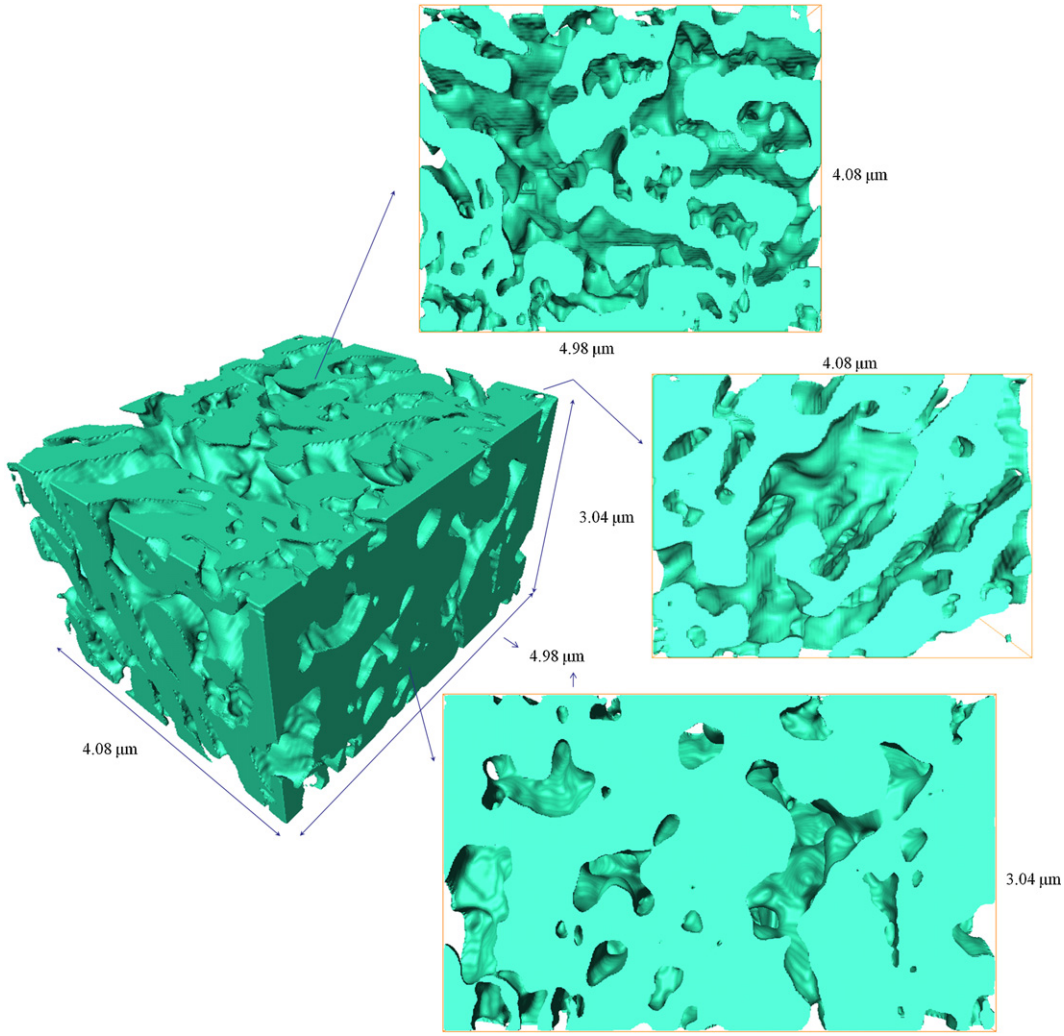

Fig. 5. Reconstructed 3D microstructure of LSM sample with 2D view of its three sides.

surfaces are bound to the void space. The coloured portion in this figure represents the pore space and the transparent part represents the LSM solid matrix. This is the 3D image of an actual pore space. Fig. 4(c) shows the 3D reconstructed image of LSM cathode with different colours assigned to the solid matrix and pores. The pore space and solid matrix of the LSM sample are easily distinguishable in this figure. Fig. 5 depicts the 3D reconstruction of the LSM sample with corresponding side views. Here the coloured part indicates the LSM solid matrix and transparent part indicates the pore space.

3.1. Impact of post-processing on the determination of microstructural properties

The different post-processing steps described previously affect the measurements of the properties of the electrode; in the following, we focus on the porosity ε and the internal surface area S. The internal surface area is calculated by counting the number of element faces at the interface between the solid and the pore phases. In the case of a Cartesian mesh, for e.g., when a 3D image is generated by stacking 2D SEM images together, counting voxel faces introduces a systematic bias. For a single sphere for instance, the surface area is overestimated by a factor 1.5 [13].

In the present analysis, firstly, the effect of the threshold value t, from a range of pixel intensity values of images of 0–255, used to discriminate the solid phase from the pore phase is presented in Fig. 6(a) for the porosity and in Fig. 6(b) for the internal surface area. Both measured quantities depend significantly on the choice of the threshold value. Between $t = 57$ and $t = 58$, the estimated porosity increases by approximately 33%. This is due to an incorrect choice of threshold, for which large portions of the image are assigned to the wrong phase. Visual inspection of a few randomly chosen slices is required to determine the proper threshold value. For the present geometry, visual inspection yields an optimal threshold value around $t = 59$ or $t = 60$. Between these two threshold values, the variation in porosity and internal surface area is only 4%.

A significant amount of noise is present in the binary images that appears as artificial pore speckles inside the solid phase. Direct application of a median filter removes the noise but tends to transform it into a large artificial pore space (indicated by red in Fig. 7). Applying a morphological opening (MO) operation [49] to the binary image beforehand significantly reduces the amount of such noise. An morphological opening is used to remove some of the pixels from the edges of regions of pore space. Fig. 8(a) and (b) shows the effect of the radius r of the median filter, with and without MO, for the porosity and the internal surface area, respectively. As expected, not applying the MO operation significantly overestimates the porosity (by about 10% for $r = 2$ pixel) and the internal surface area (by about 25% for $r = 2$ pixel). The radius of the median

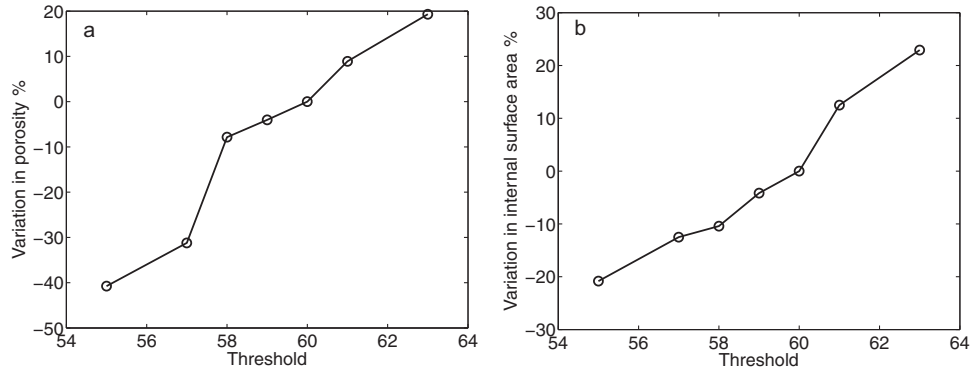

Fig. 6. Variation of measured properties as a function of the threshold value: (a) porosity and (b) internal surface area. The reference for the calculation of the variations in porosity and internal surface area is based on a threshold value of $t = 60$, a radius $r = 1$ pixel for the median filter and application of the morphological opening operation.

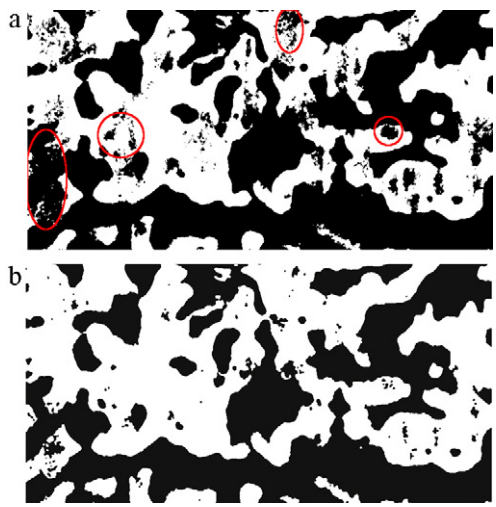

Fig. 7. Cross sectional binary images of slice number 51: (a) after applying a median filter of radius $r = 2$ pixel; (b) after applying a morphological opening and then a median filter of radius $r = 2$ pixel. The regions highlighted in red correspond to artificial pore regions generated by the filter due to the noise in the original binary images. (For interpretation of the references to colour in this figure legend, the reader is referred to the web version of the article.)

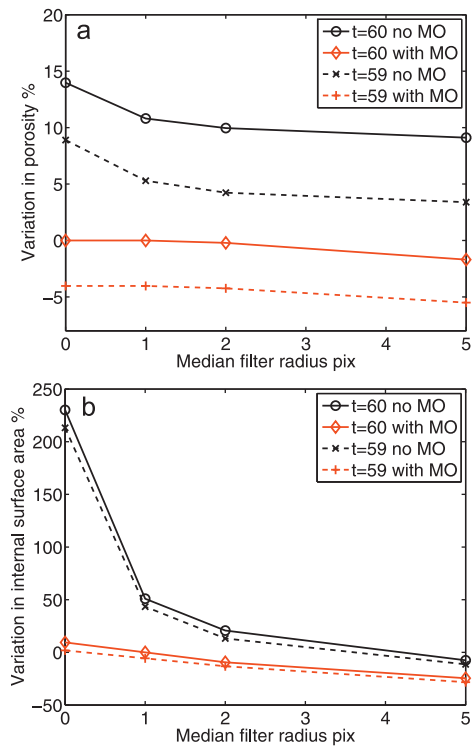

Fig. 8. Variation of measured properties as a function of radius of the median filter, with and without morphological opening: (a) porosity and (b) internal surface area. The reference for the calculation of the variations in porosity and internal surface area is based on a threshold value of $t = 60$, a radius $r = 1$ pixel for the median filter and application of the morphological opening operation.

filter does not affect the measured porosity significantly. However, the internal surface area varies by as much as 25% between a filter with a radius of 1 pixel and one with a radius of 5 pixel.

During the generation of the surface mesh, the measured geometry is interpolated. The structure-dependent properties of the material will be more or less altered, depending on the quality of the interpolation. The surface mesh (i.e., triangulation) is generated for each phase of the 3D image of 9.12 μm × 4.75 μm × 4.08 μm. Fig. 9 demonstrates the porosity (%), internal surface area (μm^2), and internal surface area density ($\mu m^2\ \mu m^{-3}$) as a function of the number of surface triangulation before and after applying smoothing filter. Fig. 9(a)–(c) clearly shows that as the number of surface triangulation of the surface mesh increases, the porosity and the internal surface area tend towards asymptotic values when the number of surface triangulation exceeds 500,000. The smoothing filter of the surface triangulation results in the internal surface area changing from 14.5% to 1.1%, as shown in Fig. 9(b) and (c), and the porosity from 4.4% to 0.03%, as shown in Fig. 9(a). Since the porosity affects the effective gas diffusivities, any changes in surface triangulation that affects porosity also affects the numerically computed effective diffusivity. Fig. 10 shows the normalized effective gas diffusivity as a function of the number of surface triangulation before and after applying smoothing filter. Fig. 10(a) – (c) shows that the normalized effective gas diffusivities in x, y, and z directions (D_x^{eff}/D, D_y^{eff}/D and D_z^{eff}/D) are asymptotically converging with the number of surface triangulation greater than 500,000.

Finally, Fig. 11 displays the normalized effective properties as a function of the number of surface triangulation after applying smoothing filter. The normalized effective electronic conductivities in x, y, and z directions, i.e., k_x^{eff}/k, k_y^{eff}/k and k_z^{eff}/k, are given in Fig. 11(a) whereas the normalized effective gas diffusivities in x, y, and z directions, i.e., D_x^{eff}/D, D_y^{eff}/D and D_z^{eff}/D, are shown in Fig. 11(b). Similar to the geometric properties, the normalized effective transport properties are asymptotically converging as the number of surface triangulation increases. It is noteworthy that the effective properties in the z-direction is significantly different than those in x- and y-direction indicating anisotropy of the overall sample or at least locally in the sample. This issue is further discussed in the Section 3.3.

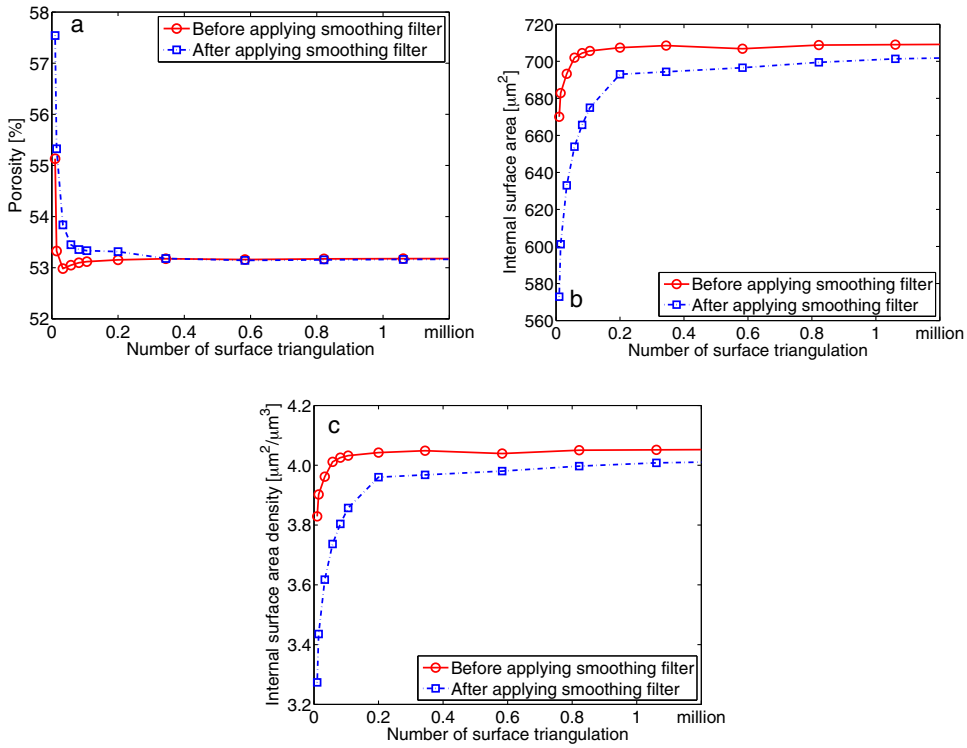

Fig. 9. Geometric properties as a function of the number of surface triangulation before and after applying smoothing filter: (a) porosity (%); (b) internal surface area (μm^2); and (c) internal surface area density ($\mu m^2\ \mu m^{-3}$).

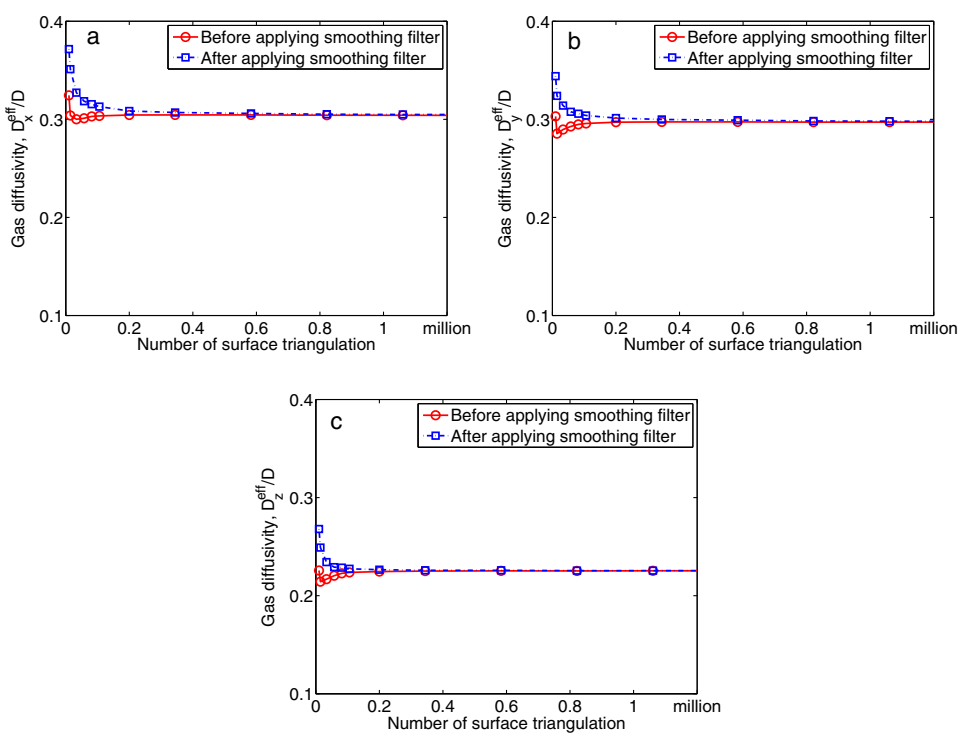

Fig. 10. Normalized effective gas diffusivity as a function of the number of surface triangulation before and after applying smoothing filter: (a) normalized effective gas diffusivity in x-direction, D_x^{eff}/D; (b) normalized effective gas diffusivity in y-direction, D_y^{eff}/D; and (c) normalized effective gas diffusivity in z-direction, D_z^{eff}/D.

3.2. Porosity and internal surface area

The total volume (pore space + LSM solid matrix) of the 3D reconstructed structure is separated into pore and LSM phase volumes through the image post-processing mentioned in the previous section. Using the threshold value of 60, the porosity (i.e., volume fraction of pore space) and the volume fraction of LSM phase are calculated as 50.6% and 49.4%, respectively. The porosity computed from the FIB-SEM sample is larger than the one estimated during the fabrication. This is likely due to the presence of

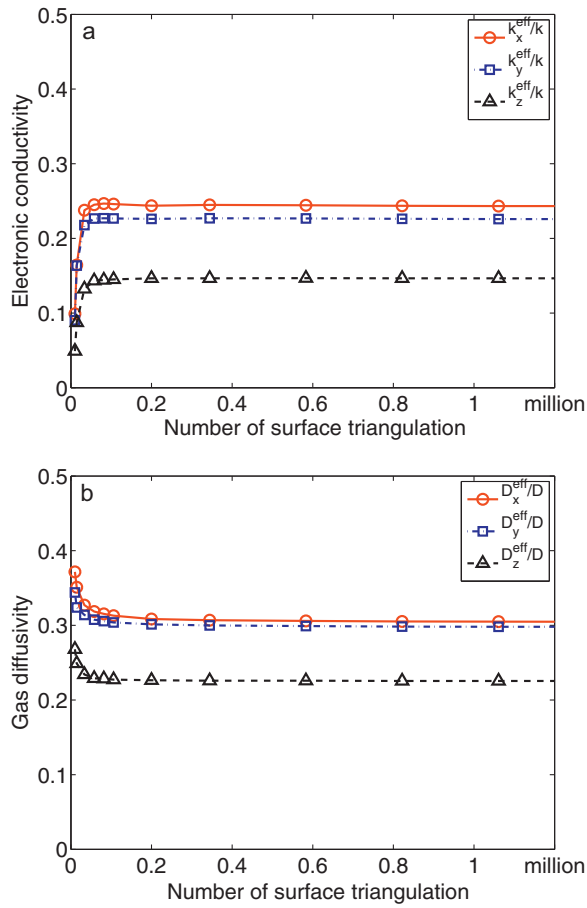

Fig. 11. Normalized effective properties in x, y, and z directions as a function of the number of surface triangulation after applying smoothing filter: (a) normalized effective conductivity in x, y, and z directions, $k^{\text{eff}}_{x,y,z}/k$ and (b) normalized effective gas diffusivity in x, y, and z directions, $D^{\text{eff}}_{x,y,z}/D$.

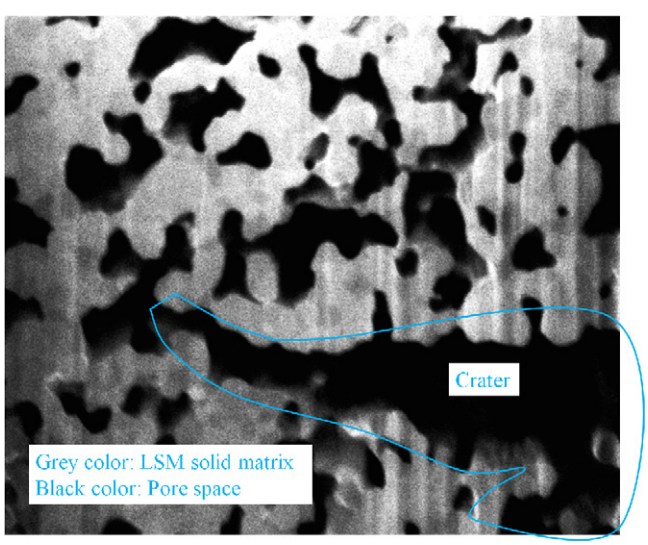

Fig. 12. Craters in the LSM sample.

crater that makes the sample more porous than expected locally. Fig. 12 shows the larger crater in the 2D cross-sectional image (slice number 94) of LSM. The gas–solid internal surface area per unit volume (i.e., the internal surface area density, S/Ω) is calculated as 4.13 $\mu m^2\ \mu m^{-3}$. Since LSM sample has only two phases, the internal surface area is the interface between pore and LSM phases.

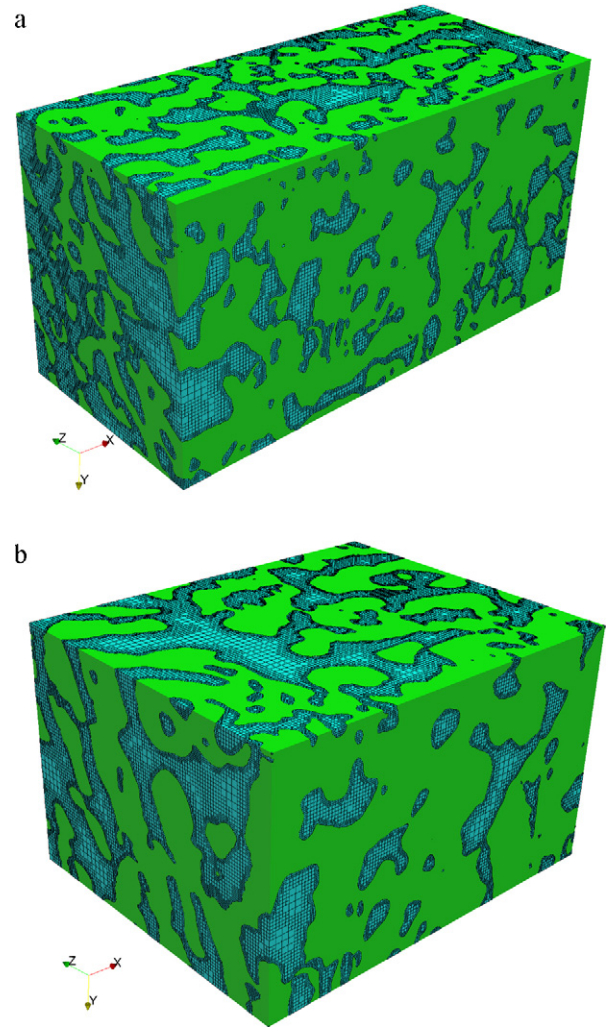

Fig. 13. 3D computational domain considered for numerical simulations to calculate the transport properties: (a) 'Sample A' has the dimension of 9.12 $\mu m \times 4.75\ \mu m \times 4.08\ \mu m$ and (b) 'Sample B' has the dimension of 4.98 $\mu m \times 3.04\ \mu m \times 4.08\ \mu m$. The green colour surface indicates LSM phase domain where as the blue colour surface with face grids denotes the pore phase domain. (For interpretation of the references to colour in this figure legend, the reader is referred to the web version of the article.)

The total surface area densities (i.e., sum of internal and boundary surface areas per unit volume) for pore and LSM phases are computed as 4.91 $\mu m^2\ \mu m^{-3}$ and 4.92 $\mu m^2\ \mu m^{-3}$, respectively. These values are comparable to those reported by Wilson et al. [8,9] who calculated the total surface areas per unit volume for a Ni:YSZ composite electrode as 3.0 $\mu m^2\ \mu m^{-3}$ for YSZ, 1.6 $\mu m^2\ \mu m^{-3}$ for Ni and 2.4 $\mu m^2\ \mu m^{-3}$ for the pore space.

3.3. Effective transport properties

Two computational domains of two different sizes are selected from the 3D reconstructed volume of the LSM and pore spaces. The 3D computational domains have the sizes of 9.12 $\mu m \times 4.75\ \mu m \times 4.08\ \mu m$ denoted as 'Sample A' and of 4.98 $\mu m \times 3.04\ \mu m \times 4.08\ \mu m$ denoted as 'Sample B'. Fig. 13 shows the computational domains required to calculate the transport properties. Fig. 13(a) and (b) displays the computational domains for Sample A and Sample B, respectively. The 3D computational domains shown in Fig. 13 were constructed by the finite volume cut-cell approach through MicroFOAM. To evaluate effective transport properties, we consider the present FIB-SEM recon-

Table 1
Normalized effective properties in x, y, and z directions based on the FIB-SEM reconstruction and the numerical reconstruction.

	Sample A		Sample B	
	FIB-SEM	Numerical	FIB-SEM	Numerical
k_x^{eff}/k	0.242	0.159	0.265	0.184
k_y^{eff}/k	0.225	0.176	0.294	0.207
k_z^{eff}/k	0.146	0.174	0.165	0.214
D_x^{eff}/D	0.304	0.298	0.276	0.265
D_y^{eff}/D	0.297	0.305	0.284	0.270
D_z^{eff}/D	0.225	0.312	0.211	0.290

structed images as well as the numerically reconstructed structures reported in Kenney et al. [3]. The numerically reconstructed electrode assumes randomly distributed LSM particles laid out to achieve a target porosity of 50%. Both reconstructed volumes are converted into the body-fitted cut-cell based finite volume meshes using the MicroFOAM [12]. The normalized effective electronic conductivity and the normalized effective gas diffusivity are calculated by Eq. (5) using both reconstruction techniques. Table 1 summarizes the normalized effective properties in x, y, and z directions calculated from two different sizes of computational domains.

Several noteworthy results can be observed from Table 1. Both the electronic conductivity and the gas diffusivity are calculated for each direction of the phase domains. It is observed that the effective properties calculated by FIB-SEM reconstruction seem to be direction dependent contrary to those evaluated by the numerical reconstruction. For the FIB-SEM reconstruction case, the normalized effective properties in z-direction, i.e., k_z^{eff}/k and D_z^{eff}/D, are roughly 25–44% smaller than the corresponding properties in x and y directions. This difference is significant and reveals the anisotropy of the measured sample. In comparison, the results for the numerically reconstructed samples vary by less than 10%. The anisotropy of the measured sample may have some bearing on the milling direction at the time of performing FIB-SEM. It is also likely due to the presence of a large crater, as observed in Fig. 12. It is to be noted that such a local feature is not taken into account in the numerically reconstructed samples. Hence, these observations question the ability of the numerical models to represent the actual structure of an electrode adequately. However, one should keep in mind that the numerically reconstructed samples are an average description of the electrode microstructure. Kenney et al. [3] recommended the use of at least 20 numerical structures in order to obtain converged values of the microstructural properties. Similarly, more samples would be necessary over which a series of FIB-SEM images are to be conducted in order to obtain properties that do not depend on local features such as cracks or large craters. However, the latter proposition is time consuming and often prohibitively expensive.

For both the actual sample reconstructed by FIB-SEM and the one created numerically, the effective properties exhibit larger variations in the three directions when the sample size is small. The importance of having a sufficiently large sample size was already acknowledged in previous experimental works by Wilson et al. [30], Iwai et al. [11], Gostovic et al. [31]. Wilson et al. [30] recommends to use a volume of at least 500 μm^3 for the sample to yield microstructural properties that are representative of the overall electrode. Additionally, Kenney et al. [3] and Metcalfe et al. [14] found that the size of the domain should be at least $14d$ or $15d$ in each direction, where d is the mean particle diameter, for the calculation of the triple-phase boundary length. For the electrode considered here, this would mean a domain volume greater than 1000 μm^3. Choi et al. [12] found that a size of $10d \times 10d \times 10d$, or 390 μm^3 in our case, is sufficient for the calculation of the effective properties. Therefore, it can be commented that the volume of the sample measured by FIB-SEM (approximately 177 μm^3) in the present study may be smaller than required based on the above arguments. One needs to be cognizant of such volume dependencies on transport properties calculated based on FIB-SEM images.

4. Conclusions

In this work, a dual-beam FIB-SEM technique was applied to reconstruct the microstructure from a porous, ceramic LSM cathode electrode material for SOFC. Preparation of LSM sample and acquisition of 2D cross-sectional images from the FIB-SEM facility was provided. Then, a formulated methodological approach was used to process the FIB-SEM 2D images for reconstructing 3D microstructures. For the first time, it was found that the image post-processing could substantially affect the geometric properties such as porosity ε and internal surface area S. The choice of threshold values as well as median filter operations affected variations of the porosity and internal surface area up to 33% and 25%, respectively. It is observed that not applying the MO operation significantly overestimates the porosity (by about 10% for $r = 2$ pixel) and the internal surface area (by about 25% for $r = 2$ pixel). The resolution of the surface triangulation used in 3D reconstructions also varied the porosity ε and internal surface area S by 14.5% and 4.4%, respectively. These variations indicate the sensitivity of imaging processing and phase segmentation methods on calculating different properties. 3D tessellation is also important and must be done with adequate resolution.

The resulting 3D reconstructed volumes were converted into the computational domains based on the body-fitted cut-cell based finite volume meshes. The normalized effective transport properties in x, y, and z directions were calculated on computational domains reconstructed by the FIB-SEM technique as well as by the numerical model. It was observed that the effective properties calculated by FIB-SEM reconstruction are more anisotropic than those evaluated by the numerical reconstruction. This local anisotropy of the measured sample was likely due to the presence of the large crater (as shown in Fig. 12) as well as a smaller sample volume used in the current FIB-SEM reconstruction. It is suggested that a large sample volume and a statistically large number of samples may remove such local anisotropy behaviour.

Acknowledgments

The authors would like to acknowledge Douglas Vick (National Research Council-National Institute for Nanotechnology) for performing the FIB-SEM on the LSM sample. The authors would also like to acknowledge the support from the Avizo(R) software courtesy of Visualization Sciences Group, Inc. The authors would like to acknowledge the hardware facilities provided by AICT visualization lab (University of Alberta) for processing the FIB data. Important discussions and support from H. Furukawa (Director, System in Frontier Inc.) are gratefully acknowledged. The authors gratefully acknowledge the financial support of Alberta Ingenuity Fund, now part of Alberta Innovates-Technology Futures from the Province of in the form of the scholarship provided to NSKG.

References

[1] L.A. Giannuzzi, F.A. Stevie, Introduction to Focused Ion Beams: Instrumentation, Theory Techniques and Practice, Springer, 2005.
[2] H.-W. Choi, A. Berson, B. Kenney, J.G. Pharoah, S. Beale, K. Karan, ECS Transactions 25 (2009) 1341–1350.
[3] B. Kenney, M. Valdmanis, C. Baker, J.G. Pharoah, K. Karan, Journal of Power Sources 189 (2009) 1051–1059.
[4] J.R. Wilson, J.S. Cronin, S. Rukes, A. Duong, D. Mumm, S. Barnett, ECS Transactions 25 (2009) 2283–2292.
[5] J.R. Wilson, A.T. Duong, M. Gameiro, H.Y. Chen, K. Thornton, D.R. Mumm, S.A. Barnett, Electrochemistry Communications 11 (2009) 1052–1056.

[6] P.R. Shearing, J. Gelb, N.P. Brandon, Journal of the European Ceramic Society 30 (2010) 1809–1814.
[7] P. Shearing, J. Golbert, R. Chater, N. Brandon, Chemical Engineering Science 64 (2009) 3928–3933.
[8] J.R. Wilson, W. Kobsiriphat, R. Mendoza, H.Y. Chen, T. Hines, J.M. Hiller, D.J. Miller, K. Thornton, P.W. Voorhees, S.B. Adler, D. Mumm, S.A. Barnett, ECS Transactions 7 (2007) 1879–1887.
[9] J.R. Wilson, W. Kobsiriphat, R. Mendoza, H.Y. Chen, J.M. Hiller, D.J. Miller, K. Thornton, P.W. Voorhees, S.B. Adler, S.A. Barnett, Nature Materials 5 (2006) 541–544.
[10] H. Ostadi, P. Rama, Y. Liu, R. Chen, X.X. Zhang, K. Jiang, Journal of Membrane Science 351 (2010) 69–74.
[11] H. Iwai, N. Shikazono, T. Matsui, H. Teshima, M. Kishimoto, R. Kishida, D. Hayashi, K. Matsuzaki, D. Kanno, M. Saito, H. Muroyama, K. Eguchi, N. Kasagi, H. Yoshida, Journal of Power Sources 195 (2010) 955–961.
[12] H.-W. Choi, A. Berson, J.G. Pharoah, S. Beale, Proceedings of the IMechE, Part A: Journal of Power and Energy, in press.
[13] A. Berson, H.-W. Choi, J.G. Pharoah, Physical Review E, submitted for publication.
[14] C. Metcalfe, O. Kesler, T. Rivard, F. Gitzhofer, N. Abatzoglou, Journal of the Electrochemical Society 157 (2010) B1326–B1335.
[15] E.L. Ritman, Annual Review of Biomedical Engineering 6 (2004) 185–208.
[16] P.R. Shearing, J. Gelb, J. Yi, W.K. Lee, M. Drakopolous, N.P. Brandon, Electrochemistry Communications 12 (2010) 1021–1024.
[17] J.R. Izzo, A.S. Joshi, K.N. Grew, W.K.S. Chiu, A. Tkachuk, S.H. Wang, W. Yun, ECS Transactions 13 (2008) 1–11.
[18] J.R. Izzo, A.S. Joshi, K.N. Grew, W.K.S. Chiu, A. Tkachuk, S.H. Wang, W. Yun, 213th ECS meeting Abstracts 2008, vol. 1, 2008, p. 275.
[19] J.R. Izzo, A.S. Joshi, K.N. Grew, W.K.S. Chiu, A. Tkachuk, S.H. Wang, W. Yun, Journal of the Electrochemical Society 155 (2008) B504–B508.
[20] J. Gelb, M. Feser, A. Tkachuk, G. Hsu, S. Chen, H. Chang, T. Fong, L. Hunter, I. Goldberger, S.H. Lau, W. Yun, Microscopy and Microanalysis 15 (2009) 618–619.
[21] S.H. Lau, W.K.S. Chiu, F. Garzon, H. Chang, A. Tkachuk, M. Feser, W. Yun, Journal of Physics: Conference Series 152 (2009).
[22] F.H Garzon, S.H. Lau, J.R. Davey, R.L. Borup, ECS Transactions 11 (2007) 1139–1149.
[23] J.R. Izzo, A.S. Joshi, K.N. Grew, W.K.S. Chiu, A. Tkachuk, S.H. Wang, W. Yun, Journal of the Electrochemical Society 155 (b504) (2008);
J.R. Izzo, A.S. Joshi, K.N. Grew, W.K.S. Chiu, A. Tkachuk, S.H. Wang, W. Yun, Journal of the Electrochemical Society 157 (2008).
[24] K.N. Grew, Y.S. Chu, J. Yi, A.A. Peracchio, J.R. Izzo, Y. Hwu, F.D. Carlo, W.K.S. Chiu, Journal of the Electrochemical Society 157 (2010) B783–B792.
[25] Y. Guan, W. Li, Y. Gong, G. Liu, X. Zhang, J. Chen, J. Gelb, W. Yun, Y. Xiong, Y. Tian, H. Wang, Journal of Power Sources 196 (4) (2011) 1915–1919.
[26] P.R. Shearing, D.J.L. Brett, N.P. Brandon, International Materials Reviews 55 (2010) 347–363.
[27] Y. Guan, W. Li, Y. Gong, G. Liu, J. Gelb, X. Zhang, Y. Xiong, Y. Tian, H. Wang, Journal of Synchrotron Radiation 17 (2010) 782–785.
[28] Y. Guan, W. Li, Y. Gong, G. Liu, X. Zhang, J. Chen, J. Gelb, W. Yun, Y. Xiong, Y. Tian, H. Wang, Journal of Power Sources 196 (2011) 1915–1919.
[29] J.R. Wilson, M. Gameiro, K. Mischaikow, W. Kalies, P.W. Voorhees, S.A. Barnett, Microscopy and Microanalysis 15 (2009) 71–77.
[30] J. Wilson, J. Cronin, A. Duong, S. Rukes, H.-Y. Chen, K. Thornton, D. Mumm, S. Barnett, Journal of Power Sources 195 (2010) 1829–1840.
[31] D. Gostovic, J. Smith, D. Kundinger, K. Jones, E. Wachsman, Electrochemical and Solid-State Letters 10 (2007) B214–B217.
[32] D. Gostovic, K. O'Hara, N. Vito, E. Wachsman, K. Jones, ECS Transactions 16 (2008) 83–93.
[33] J.R. Smith, A. Chen, D. Gostovic, D. Hickey, D. Kundinger, K.L. Duncan, R.T. DeHoff, K.S.J. amd, E.D. Wachsman, Solid State Ionics 180 (2009) 90–98.
[34] J. Joos, T. Carraro, A. Weber, E. Ivers-Tiffée, Journal of Power Sources, in press.
[35] B. Bera, S.K. Mitra, D. Vick, Micron (2010), doi:10.1016/j.micron.2010.12.002.
[36] C.L.Y. Yeong, S. Torquato, Physical Review E: Statistical Physics, Plasmas, Fluids, and Related Interdisciplinary Topics 57 (1998) 495–506.
[37] C.L.Y. Yeong, S. Torquato, Physical Review E: Statistical Physics, Plasmas, Fluids, and Related Interdisciplinary Topics 58 (1998) 224–233.
[38] P.E. Oren, S. Bakke, Journal of Petroleum Science and Engineering 39 (2003) 177–199.
[39] H. Okabe, M.J. Blunt, Journal of Petroleum Science and Engineering 46 (2005) 121–137.
[40] C. Manwart, R. Hilfer, Physical Review E: Statistical Physics, Plasmas, Fluids, and Related Interdisciplinary Topics 59: (1999) 5596–5599.
[41] P.E. Oren, S. Bakke, Transport in Porous Media 46 (2002) 311–343.
[42] W.E. LOrensen, H.E. Cline, Computer Graphics (ACM) 21 (1987) 163–169.
[43] R. Shu, C. Zhou, M.S. Kankanhalli, The Visual Computer 11 (1995) 202–217.
[44] Y. Yemez, F. Schmitt, Image and Vision Computing 22 (2004) 1137–1153.
[45] W. Ahn, J.K. Joo, H.S. Woo, D.Y. Lee, S.Y. Yi, Studies in Health Technology and Informatics 119 (2006) 1–6.
[46] T.S. Newman, H. Yi, Computers and Graphics (Pergamon) 30 (2006) 854–879.
[47] OpenFOAM®, The Open Source CFD software package, OpenCFD Ltd., London, UK, 2010, http://www.openfoam.com.
[48] P.S. Jorgensen, K.V. Hansen, R. Larsen, J.R. Bowen, Ultramicroscopy 110 (2010) 216–228.
[49] P. Soille, Morphological Image Analysis: Principles and Applications, Springer, 2003.